Induced valley splitting in monolayer MoS_2 by an antiferromagnetic insulating CoO(111) substrate

Guang Yang,[1] Jia Li,[1,2,*] Hongran Ma,[1] Yanmin Yang,[1] Congcong Li,[1] Xiujuan Mao,[1] and Fuxing Yin[2]
[1]*School of Science, Hebei University of Technology, Tianjin 300401, People's Republic of China*
[2]*Research Institute for Energy Equipment Materials, Hebei University of Technology, Tianjin 300401, People's Republic of China*

(Received 20 August 2018; revised manuscript received 27 November 2018; published 18 December 2018)

The valleytronic properties in monolayer MoS_2 induced by the magnetic proximity effect of an antiferromagnetic CoO(111) substrate have been investigated using density functional theory and Berry curvature calculations. The results show that monolayer MoS_2 can achieve a large valley splitting of 103 meV when coupled to an antiferromagnetic insulating CoO(111) substrate, which is in a robust type-II antiferromagnetic state at room temperature. The substrate provides a Zeeman field of 152 T. Breaking of the time-reversal symmetry of monolayer MoS_2 leads to a prominent anomalous Hall conductivity that has a quantized character in the range of the band edge at the K and K' valleys. Based on the result that the valley-contrasting Berry curvature is opposite at the K and K' valleys, a valleytronic device that can be used as a filter for both the valley and spin is proposed.

DOI: 10.1103/PhysRevB.98.235419

I. INTRODUCTION

In addition to electric charge and spin degrees of freedom, the valleys of the degenerate energy extremes at the special k points in the Brillouin zone (BZ) of periodic solids are considered for other distinctive electronic degrees of freedom [1–3], which can be also regarded as pseudospins. The pseudospins in different valleys are particularly robust in terms of lattice scattering because they have a large separation in momentum space. In addition to electronics and spintronics, valleytronics is a new field that concerns manipulating and using the valley index as an information carrier [4,5]. The prototype materials used to study valleytronics or valley physics are conventional semiconducting materials (e.g., Si), graphene, and monolayer transition-metal dichalcogenides (TMDs; MX_2, where M = Mo and W, and X = S and Se) [6–9]. Graphene has weak spin-orbit coupling (SOC) and the inversion symmetry for space and time are both maintained, so the spins show degenerate character at six valleys in a honeycomb k space. However, TMDs do not have space inversion symmetry because the M and X atoms occupy one of two inequivalent triangular sublattices, which leads to the neighboring two valleys, namely, K and K', no longer being equivalent. Furthermore, TMDs have strong SOC that causes spin splitting at the K and K' valleys. Owing to their exotic electronic structure, TMDs thus exhibit the carrier valley Hall effect because of the opposite sign of the Berry curvature for the K and K' valleys, and valley- and spin-dependent optical selection rules for interband transitions at the K and K' valleys [4,5,10]. In addition to the optoelectronic application potential arising from the direct band gap in the visible frequency range, monolayer TMDs, such as MoS_2 and WSe_2, have attracted a lot of research interest in nanoscience and condensed-matter physics because of the physical properties of the valleys, such as valley-selective luminescence [11,12], the valley Hall effect [13,14], and valley Zeeman splitting [15–20].

In valleytronic applications of monolayer TMDs, valley polarization between K and K' should be introduced accompanied by breaking of the time-reversal symmetry to easily distinguish and manipulate the carriers at the two valleys [3,21,22]. Two key factors to achieve valley polarization [23] are dynamic polarization (e.g., circularly polarized light) [11,24,25] and lifting the valley degeneracy by breaking the time-reversal symmetry based on introducing doping [9,26], an external magnetic field [15,17,18,24], or the magnetic proximity effect [27–33]. Although valley polarization by circularly polarized light has been theoretically investigated and also realized to some degree experimentally [4–7,11,24,25], the method of optical pumping is not suitable for valleytronic applications owing to the difficulty in control. Alternative approaches to lift the valley splitting are by introducing a magnetic field to the monolayer TMD, doping magnetic moments into the monolayer TMD, and establishing a heterostructure by coupling a magnetic substrate with the monolayer TMD. The latter approach has proven to be particularly effective both theoretically and experimentally [27–35]. Biaxial strain, an electric field, and the distance of the Zeeman effect are valid strategies to manipulate and modulate valley splitting [28,30,33–37].

The large valley splitting induced by antiferromagnetic insulating substrates is slightly strange because macroscopically they have zero magnetization. However, the magnetic proximity effect still occurs because the magnetic layer neighboring the monolayer TMD has a uniform moment, which still exerts a ferromagnetic local field at the interface. In general, antiferromagnetic materials have higher Curie temperatures than ferromagnetic materials. Therefore, it is desirable to search for antiferromagnets that are suitable for substrate coupling to monolayer TMDs. CoO is in a robust antiferromagnetic state at room temperature [38] and monolayer MoS_2 on the

*jiali@hebut.edu.cn

CoO(111) substrate exhibits a small lattice mismatch. Moreover, CoO shows a (111) preferred orientation [39,40], which means that monolayer MoS_2 can easily epitaxially grow on the CoO(111) substrate.

Here, we performed density functional theory (DFT) and Berry curvature calculations to explore the valley-splitting-related properties induced by the magnetic proximity effect by coupling the CoO(111) substrate with monolayer MoS_2. The results show that the valley splitting of MoS_2 at the K and K' valleys is lifted to 103 meV owing to the magnetic proximity effect caused by the antiferromagnetic insulating CoO substrate, which is in contrast to the nonvalley splitting of freestanding MoS_2. The Berry curvature has opposite signs at the K and K' valleys and the anomalous Hall conductivity (AHC) is nonzero when shifting the Fermi level between the two valley extrema, which indicates that a valleytronic device can be designed to realize the valley-polarized anomalous Hall effect and filter carriers with certain spin and valley indexes.

II. METHODOLOGY

The DFT calculations for structural relaxation and electronic structure were performed by using the Perdew-Burke-Ernzerhof generalized gradient approximation (PBE-GGA) for the exchange and correlation function as implemented in the Vienna ab initio simulation package (VASP) [41–44]. The electron-ion interaction was described by the projector augmented wave (PAW) potentials [45,46]. The cutoff energy for the plane-wave expansion was set as 500 eV. The Brillouin zone (BZ) integrations were performed using a $10 \times 10 \times 1$ Monkhorst-Pack k mesh for total-energy calculations. During the structural relaxation, the energy convergent criterion was 10^{-5} eV per unit cell, and the forces on all relaxed atoms were less than 0.01 eV/Å. The DFT-D2 dispersion correction method was included in the structural relaxation and electronic structure calculations to correctly describe the effect of van der Waals integrations [47]. Spin-orbit coupling was not included during the structure relaxations to save computation resources while considering the electronic structure calculations. In the structural model of MoS_2/CoO heterostructure, a vacuum space of 20 Å was added along the z direction (in the direction perpendicular to the interface) to decouple the spurious interaction between repeated slabs. In our study, the DFT+U formalism was used to account for the strong on-site Coulomb repulsion for CoO, and the Coulomb and exchange parameters U and J were set to 8.9 and 1.0 eV for the d orbital of Co atoms, respectively (see Sec. III A).

For the calculation of Berry curvature and anomalous Hall conductivity of the MoS_2/CoO heterostructure, we used the maximally localized Wannier function method, as implemented in the WANNIER90 package [48], to construct real-space maximally localized Wannier functions (MLWFs) after obtaining the self-consistent ground state of the system under study. The initial orbital projections for iterative MLWFs minimization were based on Mo-s:p:d, S-s:p, Co-s:p:d, and O-s:p, and that the calculated Wannier functions had been sufficiently localized.

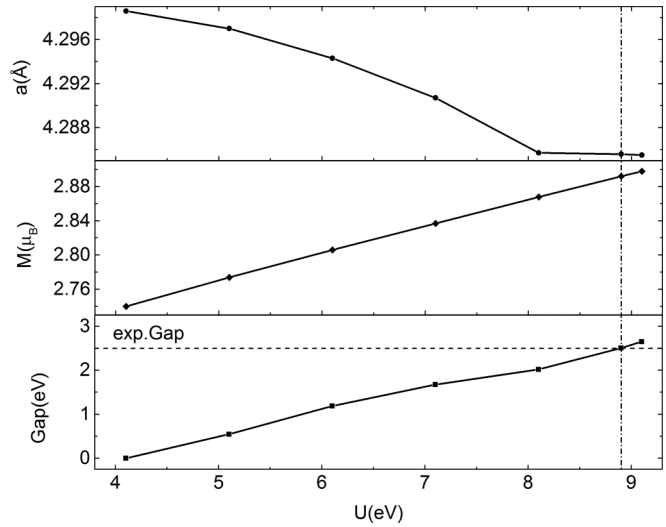

FIG. 1. Lattice constant a, magnetic moment M, and the band-gap dependence upon the Coulomb parameter U for GGA+U calculations. The vertical dashed line represents the U value, with which the calculated band gap is in good agreement with the experimental value of the band gap marked by the horizontal dashed line.

III. RESULTS AND DISCUSSION

A. Structural properties of MoS_2/CoO heterostructure

The monolayer MoS_2 we used has a 2H structure. It was fabricated from the corresponding 2H phase bulk material with honeycomb hexagonal lattice structure (space group $P6_3/mmc$) by mechanical exfoliation [49], and its lattice constant is 3.15 Å [50]. CoO is a cheap octahedron oxide of cobalt and has a rock-salt structure (space group $Fm3m$), which includes two interpenetrating face-centered-cubic sublattices occupied by Co and O atoms. It is a type-II antiferromagnetic (AFM) insulator at room temperature with a Neel temperature of 298 K [38]. This type-II AFM order indicates that the magnetic moment of every Co atom is opposite to that of all of the neighboring Co atoms. However, in the (111) plane of CoO, the magnetic moments of Co atoms in every layer have the same direction, while those of the two adjacent layers have the opposite moment direction. The on-site Coulomb parameter for the DFT+U calculation of CoO has been determined by Wdowik and Parlinski to be $U = 7.1$ eV and $J = 1$ eV using the PW91 exchange-correlation (xc) functional [51]; however, it is significant and necessary to test this parameter for a proper description of the ground state of CoO in the present work because we used the PBE xc functional. The test calculations were performed for a range of U values, from 4.1 to 9.1 eV, and the effects of varying U on the lattice constant, magnetic moment, and band gap are shown in Fig. 1. It was found that the lattice constant and magnetic moment showed a weak dependence on the U value, while the band gap was sensitive to U. We concluded that the values of $U = 8.9$ eV and $J = 1$ eV were suitable to be used in the further calculations for the electronic structure because the obtained calculated band gap of 2.51 eV agreed well with the experimental value of 2.5 eV [52]. In addition, the calculated lattice constant of the cobalt atom using this U value was 4.28 Å, which was in good agreement with the experimental value of 4.26 Å (0.5%

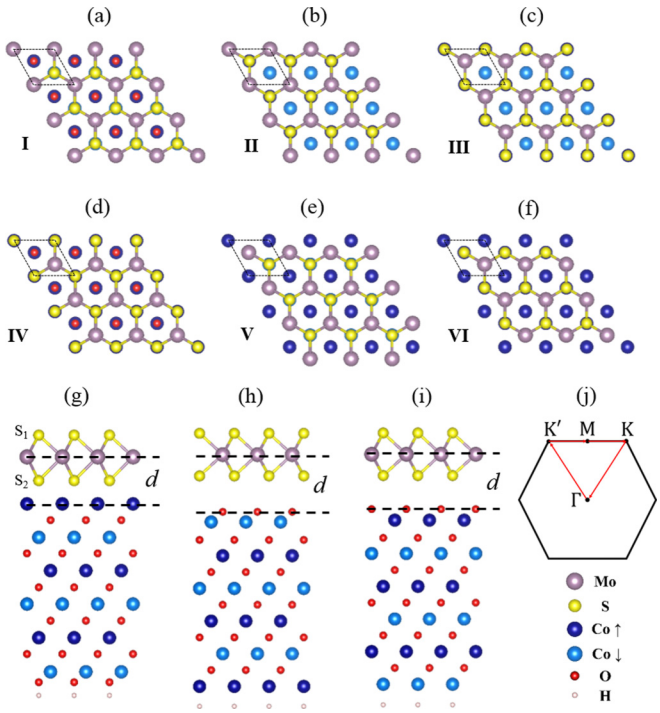

FIG. 2. (a)–(f) Top views of the six configurations I–VI of the MoS_2/CoO(111) heterostructure for the Co-terminated substrate. Side views of MoS_2/CoO(111) heterostructure in configuration I for (g) Co-terminated and (h),(i) O-terminated substrates. (j) Brillouin zone with the high-symmetry points.

deviation) [52]. As a result, the hexagonal CoO(111) surface had an optimized lattice constant of 3.03 Å with a 0.6% deviation compared with the experimental value of 3.01 Å. We constructed the MoS_2/CoO(111) heterostructure by coupling monolayer MoS_2 to the CoO(111) slab substrate, where the lattice was fixed and a small compressive strain was added to the monolayer MoS_2. Thus, the lattice mismatch between monolayer MoS_2 and the CoO(111) slab substrate was 3.94% based on the calculated lattice constant of CoO, and 4.58% based on experimental lattice constant of CoO.

As shown in Fig. 2(g), we constructed the CoO(111) slab including 12 atomic layers for the Co-terminated substrate by taking into account the symmetry and considering the computational resources. In the structural optimization of the slab, we only considered relaxation of the top four atomic layers to obtain the precise geometry of the slab model and reduce the computational workload. To avoid dangling bonds of the O atoms on the bottom surface, we saturated the structural model with H atoms.

We investigated six possible configurations of the MoS_2/CoO(111) heterostructure, named as configurations I–VI, by considering the high-symmetry positions, as shown in Figs. 2(a)–2(f), respectively; namely, the topmost Co or O atoms of the CoO substrate directly below the Mo atoms, S atoms, or hexagonal hollow sites of the MoS_2 monolayer along the vertical direction of the interface. In the calculations, the DFT-D2 dispersion correction method was used for the van der Waals interactions between the MoS_2 monolayer and the CoO substrate, as mentioned in the calculation details.

TABLE I. Calculated interfacial distances d, band gaps, binding energies, and magnetic moments of monolayer MoS_2 and surface Co for the six configurations of the MoS_2/CoO(111) heterostructure.

	I	II	III	IV	V	VI
d (Å)	3.52	3.55	3.92	3.97	3.56	3.58
Gap (eV)	0.74	0.53	0.55	0.42	0.77	0.76
E_b(eV)	−4.65	−4.21	−3.94	−3.89	−4.45	−4.29
$\mu_{S_1}(\mu_B)$	0.011	−0.002	−0.018	−0.004	0.006	0.00
$\mu_{S_2}(\mu_B)$	0.029	0.021	−0.022	−0.015	0.02	0.009
$\mu_{Mo}(\mu_B)$	0.044	−0.098	−0.176	−0.116	0.022	−0.102
$\mu_{Co\text{-surface}}(\mu_B)$	2.775	2.698	2.819	2.441	2.796	2.709

After structural relaxation, the atomic positions and bond lengths at the interfaces were slightly different from those of the original structure.

We calculated the binding energies of the six configurations by

$$E_b = E_{MoS_2/CoO} - E_{MoS_2} - E_{CoO}, \quad (1)$$

where $E_{MoS_2/CoO}$, E_{MoS_2}, and E_{CoO} are the total energies of the heterostructure, MoS_2 monolayer, and CoO slab, respectively. The calculated results are listed in Table I, where a negative binding energy indicated that the heterostructure can stably exist. Configuration I (i.e., eclipsed stacking with Mo atoms over Co atoms and the hexagonal hollow sites of the MoS_2 monolayer over O atoms) was the most stable structure. For a two-dimensional (2D) crystal, the strain energy can be expressed as

$$U(\varepsilon) = \tfrac{1}{2}C_{11}\varepsilon_{xx}^2 + \tfrac{1}{2}C_{22}\varepsilon_{yy}^2 + C_{12}\varepsilon_{xx}\varepsilon_{xy} + 2C_{44}\varepsilon_{xy}^2. \quad (2)$$

The Born-Huang criteria, namely, $C_{11}C_{22} - {C_{12}}^2 > 0$ and $C_{44} > 0$, can be used to check the mechanical stability [53]. Therefore, we also calculated the elastic constants of configuration I, and the calculated values for C_{11}, C_{12}, C_{22}, and C_{44} were 161.65, 43.73, 167.50, and 23.51 GPa, respectively. These values satisfied the Born-Huang criteria, which suggested that configuration I was mechanically stable.

The calculated interfacial distance d, band gap, and magnetic moment of each atom of the MoS_2 monolayer and interfacial Co atoms for the six configurations are listed in Table I. We defined d as the distance between the surface Co or O atoms and the Mo atoms, which is shown in Figs. 1(g)–1(i). The results revealed that the stacking configurations have a great influence on the interfacial distance and energy gap. Configurations I and IV had the smallest d value of 3.52 Å and largest d value of 3.97 Å, respectively, that is, the most stable configuration I had the smallest interfacial distance. The energy gap varied in the range 0.42–0.77 eV, and was 0.74 eV for configuration I. The magnetism of MoS_2 induced by the magnetic CoO substrate was also sensitive to the configuration, and the directions and magnitudes of the moments of the Mo and S atoms for the six configurations were slightly different. It was also observed that the induced magnetism of the transition-metal atoms by the magnetic CoO substrate was larger than the chalcogen atoms, and the magnetism of the inner-layer chalcogen atoms was larger than the outer-layer

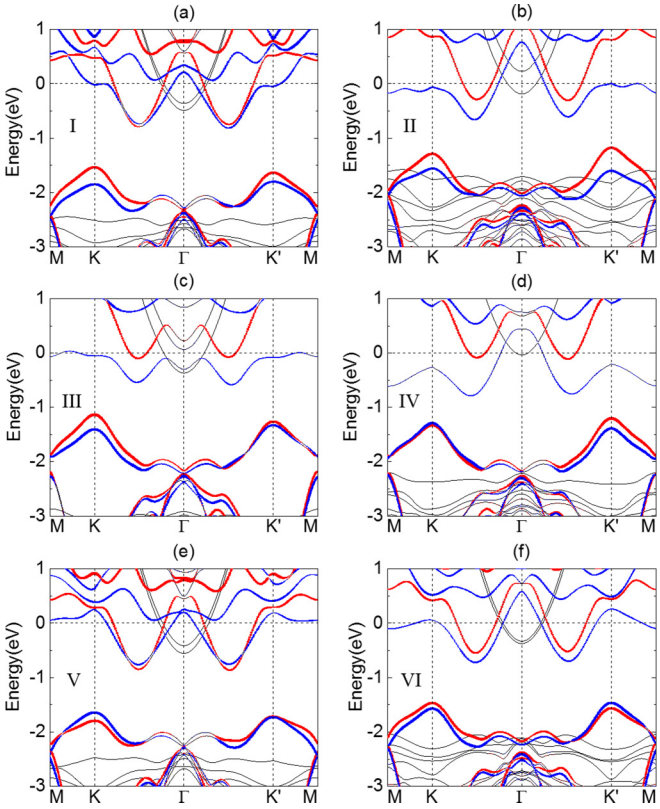

FIG. 3. Calculated band structures of the six configurations I–VI of the MoS_2/CoO(111) heterostructure for the Co-terminated substrate. The spin projections for the MoS_2 monolayer are represented by red and blue lines. The sizes of the red and blue solid circles represent the weight of the up- and down-spin states of MoS_2, respectively. The Fermi level is set to zero and indicated by the black dashed line.

atoms. For configuration I, the atomic moments of Mo, top S [S_1 in Fig. 1(g)], and bottom S [S_2 in Fig. 1(g)] atoms were 0.044 μ_B, 0.011 μ_B, and 0.029 μ_B, respectively, which indicated a weak ferromagnetic coupling. More interestingly, the MoS_2 monolayer also showed weak ferromagnetic coupling with the interfacial Co atoms, which indicated that the antiferromagnetic insulating CoO substrate not only broke the time-reversal symmetry, but it also introduced magnetism to the nonmagnetic MoS_2 monolayer.

B. Electronic and valleytronic properties of MoS_2/CoO heterostructure

The MoS_2-weighted band structures with SOC for the six MoS_2/CoO(111) configurations are shown in Fig. 3. The z axis was chosen as the quantized direction, and the spin-up and spin-down projected states of the MoS_2 monolayer are indicated by the red and blue circles, respectively, where the diameter was proportional to the weight of the state at that k point. We first give a general description of the electronic band structure and a detailed discussion of the valley and spin splitting will be given in the next paragraph. First, the Fermi level of all of the configurations shifted into the conduction band owing to charge transfer from the CoO substrate, in contrast to freestanding MoS_2. However, the semiconducting

TABLE II. Energies of the top valence bands and the spin splitting at K and K' for each spin of configurations I–VI of the MoS_2/CoO(111) heterostructure.

	I	II	III	IV	V	VI
$E^+_{v,K}$(eV)	−1.53	−1.29	−1.13	−1.34	−1.80	−1.47
$E^-_{v,K}$(eV)	−1.85	−1.57	−1.40	−1.30	−1.64	−1.57
$E^+_{v,K'}$(eV)	−1.62	−1.81	−1.27	−1.20	−1.72	−1.57
$E^-_{v,K'}$(eV)	−1.81	−1.91	−1.34	−1.40	−1.74	−1.46
δ(eV)	0.32	0.28	0.27	0.04	0.16	0.10
δ'(eV)	0.19	0.10	0.07	0.20	0.02	0.11

character of MoS_2 in the six configurations was preserved because all of the band structures showed a clear band gap in the range 0.42–0.77 eV (Table I). Configuration I had a band gap of 0.74 eV, which was smaller than the band gap of 1.6 eV for freestanding monolayer MoS_2. Freestanding monolayer MoS_2 had a direct band gap at the K point, but the band gap of MoS_2 in the six heterostructures changed to indirect because of hybridization with the states of the substrate. The valley character of the conduction band was lost because the conduction-band minimum (CBM) shifted to $\Gamma \rightarrow K$ or $\Gamma \rightarrow K'$. However, the valence-band maximum (VBM) located at K or K' showed a prominent valley character, and spin splitting clearly occurred in the two valleys owing to strong SOC. For comparison, the energies of the top valence bands of the six configurations for spin up and down are given in Table II. The parameters δ and δ' denote the energy difference between the K and K' valley extrema of the topmost and second-topmost valence bands, respectively, which can be called spin splitting. The valley splitting was robust because δ and δ' were large (20–320 meV) for all of the configurations. The spin splitting for configuration I was 320 meV at the K valley and 190 meV at the K' valley, and the following discussion will be based on this structural model.

To reveal the contributions of the different atomic states in the band edge, the total and atomic spin-polarized density of states (DOS) of MoS_2/CoO are shown in Figs. 4(a) and 4(b). First, we will focus on the total DOS [Fig. 4(a)]. For the spin-up states, the VBM exclusively came from MoS_2. However, for the spin-down states, the VBM came from the strong hybridized states of MoS_2 and CoO. Differing from the VBM, the CBM had contributions from both MoS_2 and CoO (i.e., hybridized states). To obtain a better understanding of the orbital contributions of Mo and S atoms to the VBM, the orbital-resolved DOS for Mo and S atoms are shown in Fig. 4(b). For the spin-up DOS of the VBM, there was strong hybridization between the Mo d and S p orbitals. In addition, there was strong hybridization between the Mo d and S p orbitals in the entire energy range. To further explore this point, the orbit-weighted bands of the five d orbitals of Mo and three p orbitals of S around the VBM along $M \rightarrow K$ and $M \rightarrow K'$ are shown in Figs. 4(c) and 4(d). At the K and K' points, the VBM was mainly composed of the Mo d_{xy} and $d_{x^2-y^2}$ states. By shifting to the M point, the contributions of other orbital states become larger, and at the M point, all of the states are dominated by the S p_y and p_x states. This variation of the contributions of the Mo d_{xy} and $d_{x^2-y^2}$ states was similar

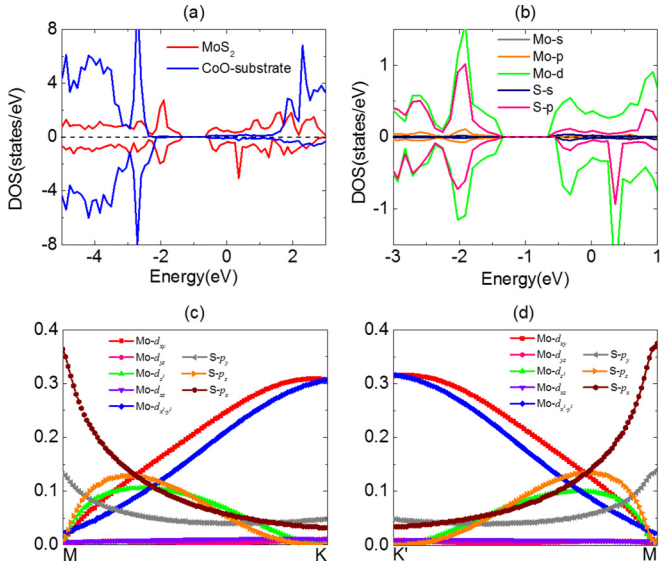

FIG. 4. (a) DOS of the MoS_2/CoO(111) heterostructure for the Co-terminated substrate. (b) Orbital-resolved DOS for Mo and S. The upward and downward lines represent the up- and down-spin states, respectively. The energy zero denotes the Fermi level. Orbit-weighted bands for the five d orbitals of Mo and three p orbitals of S around the VBM along the lines (c) M to K and (d) K' to M. The ordinate represents the relative contribution of the orbital.

to that for the spin splitting because spin splitting also showed an increasing trend along M–K and $M - K'$. Therefore, we concluded that the Mo d_{xy} and $d_{x^2-y^2}$ states around the K and K' points play a key role in the spin splitting.

To describe the valley-splitting property of monolayer TMDs, the following two-band theoretical model has been proposed in terms of $k \cdot p$ perturbation at the K and K' valleys [4]:

$$H_0 = at(\tau k_x \hat{\sigma}_x + k_y \hat{\sigma}_y) + \frac{\Delta}{2}\hat{\sigma}_z - \lambda\tau\frac{\hat{\sigma}_z - 1}{2}\hat{s}_z, \quad (3)$$

where a, t, Δ, and 2λ are the lattice constant, effective hopping integral, energy band gap, and SOC strength, respectively. τ is the valley index, which is $+1$ and -1 for the K and K' valleys, respectively. $\hat{s}_z$ is the spin operator, which has two eigenvalues of $+1$ and -1. $\hat{\sigma}$ are the Pauli matrices for the two base functions:

$$|\phi_c\rangle = |d_{z^2}\rangle, \quad |\phi_v^\tau\rangle = \frac{1}{\sqrt{2}}(|d_{x^2-y^2}\rangle + i\tau|d_{xy}\rangle), \quad (4)$$

where the subscript c (v) denotes the conduction (valence) band [4]. The reason for choosing these two bases was that the VBM mainly arises from the contributions of the Mo d_{xy} and $d_{x^2-y^2}$ states and the CBM arises from the contribution of Mo dz^2, as mentioned above. The magnetic proximity of CoO exerted on the MoS_2 monolayer that caused an additional Zeeman energy term is

$$H_1 = m\hat{s}_z, \quad (5)$$

where m is the effective exchange field. By fitting the above Hamiltonian to the calculated DFT band structure, we could obtain all of the parameters of the Hamiltonian. We define the spin splitting as

$$\Delta_{\text{split}} = 2\lambda + \Delta_m, \quad (6)$$

where Δ_{split} is the total spin splitting at the K or K' valley, and 2λ and Δ_m are the spin splitting caused by SOC and the exchange field, respectively. This definition was based on the fact that H_0 well describes the spin splitting at the K and K' valleys for freestanding monolayer MoS_2 [4] and the magnetic proximity effect will introduce spin polarization to monolayer MoS_2 on a magnetic substrate, and thus lead to additional spin splitting as well as prominent valley polarization owing to strong spin-valley coupling. Thus, it was reasonable to divide the total spin splitting into these two parts. For comparison, the valence-band structures with SOC for freestanding monolayer MoS_2 and the MoS_2/CoO heterostructure, as well as the theoretical valence bands using the above Hamiltonian model, are shown in Figs. 5(a)–5(c). From Fig. 5(a), for the freestanding monolayer MoS_2, spin splitting occurred at both the K and K' valleys, and the spin direction was opposite. Moreover, the two valleys had the same splitting magnitude of 0.15 eV, that is, $2\lambda = 0.15$ eV. As shown in Fig. 5(b), monolayer MoS_2 on the magnetic CoO substrate showed a larger spin splitting at the K and K' valleys than freestanding monolayer MoS_2, where $\Delta_{\text{split}} = 0.32$ eV at the K valley and $\Delta_{\text{split}} = 0.19$ eV at the K' valley. Therefore, the Δ_m values for the K and K' valleys were 0.17 and 0.04 eV, respectively. Figure 5(c) shows the result of the above Hamiltonian model [Eq. (6)] with the lattice constant a set to the optimized value of 3.03 Å, $2\lambda = 0.15$ eV, and $\Delta = 0.74$ eV, that is, the band gap of MoS_2 on the magnetic CoO substrate [see Fig. 3(a)]. The remaining two parameters, that is, the effective hopping integral t and effective exchange field m, were determined to be 0.18 eV and 8.8 meV, respectively, by fitting the theoretical bands to the DFT bands. The effective

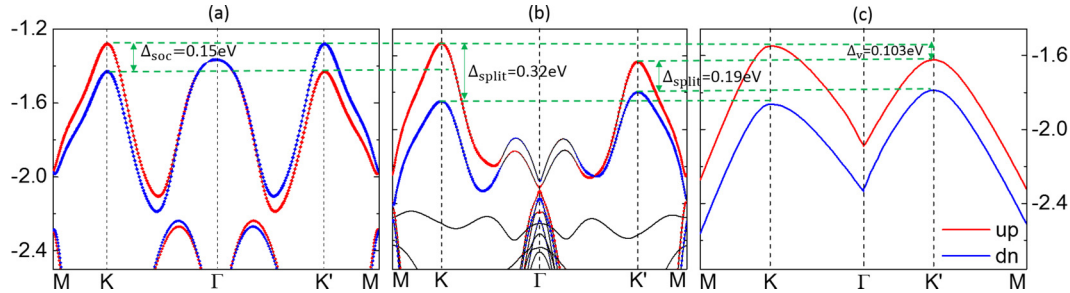

FIG. 5. Valence-band structures of (a) freestanding MoS_2 and (b) MoS_2/CoO calculated by DFT. (c) Theoretical valence structure of MoS_2 on the CoO substrate from the Hamiltonian model, which has been best fitted to the DFT band by modulating the model parameters.

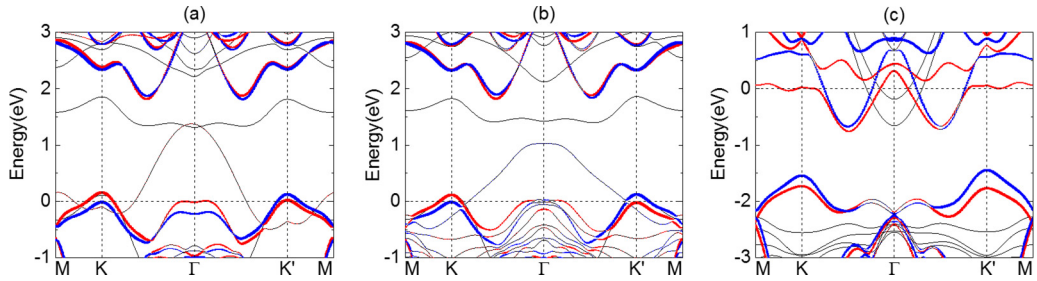

FIG. 6. (a),(b) Calculated band structure of the MoS_2/CoO(111) heterostructure for two O-terminated CoO(111) slabs. (c) Calculated band structure of configuration I, in which the moment direction of interfacial Co atoms has been reversed.

exchange field of 8.8 meV was equal to a magnetic field of 152 T because one Bohr magneton is equal to 5.78×10^{-5} eV T^{-1}. This magnetic exchange field caused spin splitting besides the SOC-induced splitting, and an inequivalent splitting of the K and K' valleys (i.e., valley polarization is achieved). We defined the valley splitting Δ_v as the energy difference between the two valley extrema, and $\Delta_v = 103$, as shown in Fig. 5(c). If the Fermi level shifts to the middle of the valence edge of K and K' by doping or other approaches, the spin- and valley-characterized carriers can be detected by circularly polarized light or spin-polarized scanning tunneling microscopy [28].

C. Structural, electronic, and valleytronic properties of MoS_2/CoO heterostructure for O-terminated CoO substrate

We also calculated the electronic structure of the MoS_2/CoO heterostructure with an O-terminated CoO substrate [Figs. 6(a) and 6(b)]. These structural models were based on configuration I, but the interfacial atoms neighboring the MoS_2 monolayer were O atoms rather than Co atoms. Considering the moment direction of Co, we constructed two O-terminated CoO(111) slabs with 12 layers: eclipsed stacking with the Mo atoms above O atoms and the hexagonal hollow sites of the MoS_2 monolayer above Co atoms, as shown in Figs. 2(h) and 2(i), respectively. The calculated d values for these two O-terminated heterostructures were 4.11 and 4.09 Å, respectively. These values were larger than those of the Co-terminated heterostructures, which indicated that the O-terminated heterostructures were more weakly coupled to the MoS_2 monolayer. Compared with the band structures of the Co-terminated heterostructures shown in Fig. 3, the O-terminated heterostructures only exhibited a small valley splitting and had some interfacial states in the band gaps, which would inhibit valleytronic applications. In addition, the O-terminated heterostructures were unstable because their calculated binding energies were both positive. Therefore, the Co-terminated heterostructures were more suitable for valleytronic devices than the O-terminated heterostructures, although the latter also showed valley-splitting character.

D. Berry curvature and anomalous Hall conductivity of MoS_2/CoO heterostructure

The Berry curvature-induced intrinsic transverse velocity shows the physical nature of the anomalous Hall effect. It also leads to the so-called valley Hall effect for TMDs because the Berry curvature in the valence or conduction band is opposite for K and K' valleys [54]:

$$\Omega(k) = \pm \frac{2\tau a^2 t^2 (\Delta - \tau s_z \lambda)}{\left[(\Delta - \tau s_z \lambda)^2 + 4a^2 t^2 k^2\right]^{\frac{3}{2}}}, \tag{7}$$

where the valley order τ has opposite signs for the two valleys, and the + and - signs represent the valence and conduction band, respectively. The integral of the Berry curvature over the occupied states gives the contribution to the Hall conductivity [54]:

$$\sigma_H = \frac{e^2}{\hbar} \sum \int \frac{d^2k}{(2\pi)^2} f(k, \tau, s_z) \Omega(k, \tau, s_z), \tag{8}$$

where f is the Fermi-Dirac distribution function. In the absence of a magnetic field, the net effect is a pure valley Hall current with a vanishing charge Hall current. However, an additional magnetic field will cause a net charge current because the Hall currents from the two valleys do not completely cancel [54]. Here, the magnetic exchange field of the CoO substrate exerted on MoS_2 was expected to cause quantized anomalous Hall conductivity owing to the broken time-reversal symmetry. A practical computational method for Berry curvature and Hall conductivity has been developed, namely, the Wannier interpolation, which is based on the well-constructed MLWFs instead of summation over all the occupied and unoccupied states [55], and the calculated Berry curvature using Wannier interpolation was in good agreement with the results by Yugui Yao *et al.* [56], who used the bare DFT calculation with 20 000 k points. Therefore, we calculated the Berry curvature and anomalous Hall conductivity (AHC) for the MoS_2/CoO heterostructure based on DFT calculations in combination with the MLWFs shown in Figs. 7(b)–7(d). To ensure the calculation accuracy of the Wannier base functions, we first plotted the tight-binding band structure using the MLWFs shown in Fig. 7(a). We found that the band dispersion coincided well with the DFT result [Fig. 2(a)], which indicated that the produced Wannier base functions were sufficiently localized and the accuracy of the calculation was ensured. The Berry curvature as a contour map over the 2D BZ and as a curve along the high-symmetry points with the Fermi level located inside the band gap are shown in Figs. 7(b) and 7(c), respectively. The Berry curvatures for the K and K' valleys had the same absolute value but opposite signs, which suggested that the magnetic proximity effect induced by CoO did not break the valley-contrasting characteristic of monolayer MoS_2. The

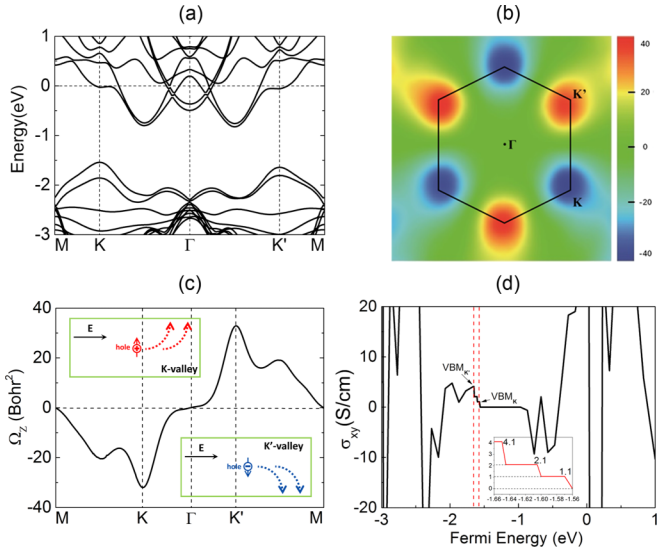

FIG. 7. (a) Band structure calculated by MLWFs. (b) Contour map of the Berry curvature in the 2D BZ. (c) Berry curvature along the high-symmetry points of the BZ for the Fermi level located inside the band gap. The insets show the anomalous Hall effects for the K and K' valleys. (d) AHC with the Fermi level in the same energy range as the band structure. The inset shows a plot in which the Fermi level is between the VBM of K' and the VBM of K.

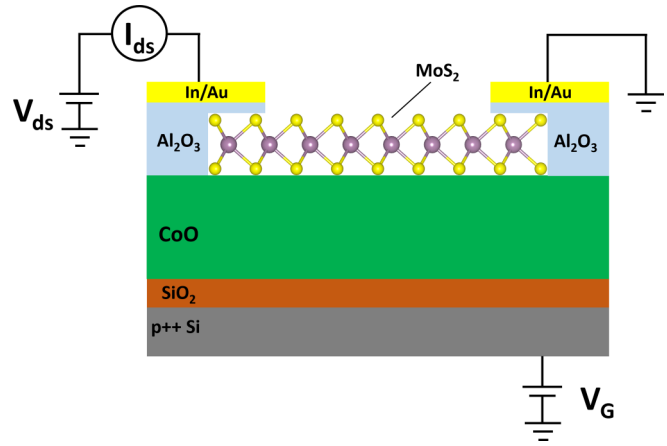

FIG. 8. Schematic of the monolayer MoS_2/CoO(111) heterojunction for valleytronic devices.

calculated AHC plotted against the Fermi level in the same energy range as the band structure is shown in Fig. 7(d), where the two dashed lines denote the VBMs at the K' and K valleys. The valley-polarized character of the AHC was prominent because it changed from a small finite value to zero when the Fermi level shifted from -1.53 eV (VBM of K) to -1.62 eV (CBM of K'). For further investigation, we replotted the AHC against the Fermi level in the range between the two valleys [inset of Fig. 7(d)]. This showed that the AHC exhibited a step feature with three plateaus at 1.1, 2.1, and 4.1 $\mathrm{S\,cm^{-1}}$, which indicated that it was quantized. The quantized Hall conductivity for magnetic bands has been reported theoretically based on the 2D electron gas formalism [57] and the semiclassical equations for electrons in magnetic Bloch bands [56,58].

Based on the calculated results of the Berry curvature and AHC for the monolayer MoS_2/CoO(111) heterostructure, a valleytronic device could be constructed. A schematic of the device is shown in Fig. 8. This device can be used to realize the valley-polarized anomalous Hall effect and filter carriers with certain spin and valley indexes. The average velocity of electrons in an electric field is given by [2]

$$\upsilon_n(k) = \frac{\partial \varepsilon_n(k)}{\hbar \partial k} - \frac{e}{\hbar} E \times \Omega_n(k), \tag{9}$$

where $\Omega_n(k) = i\langle \nabla_k u_n(k)| \times |\nabla_k u_n(k)\rangle$ is the Berry curvature of the Bloch state for the nth band. The first term is the band-dispersion contribution, and the second term is the so-called anomalous velocity that is transverse to the extra electric field. By doping or other approaches, the Fermi level can be tuned between the VBMs of the K and K' valleys. If an in-plane longitudinal electric field is then applied to the device, the holes at the K and K' valleys will achieve opposite transverse velocity owing to the opposite signs of their Berry curvature, as mentioned above [4]. An illustration of the carrier movement is shown in the insets of Fig. 7(c), where the plane corresponds to the xy plane of the MoS_2/CoO(111) heterostructure. Compared with the band structure shown in Fig. 3(a), the carriers are spin-up holes at the K valley and they will move toward the upside owing to the negative Berry curvature at the K valley, as shown in the upper inset of Fig. 7(c). If the magnetic ordering of the outermost-layer Co atoms coupled with the monolayer MoS_2 is reversed from up to down, of which the band structure is provided in Fig. 6(c), the spin-down holes at the K' valley will become carriers and they will have downside transverse velocity owing to the positive Berry curvature, as shown in the lower inset of Fig. 7(c). The hole carriers with K or K' nature will accumulate at one transverse edge of the device, and then a sizable voltage can be measured owing to the anomalous Hall effect. In particular, the hole carriers near the Fermi level possess up spin for both the K and K' valleys, as shown in Fig. 3(a). Thus, this device can also be used as a spin filter to filter all of the carriers with up spin to move transversely, which will generate a Hall current. This MoS_2/CoO-based heterojunction could potentially be used as a valleytronic device for the anomalous Hall effect as both a spin and valley filter, where the transport carriers could move in a horizontal plane by adding an in-plane longitudinal electric field.

IV. CONCLUSION

We have performed DFT and Berry curvature calculations to show that prominent valley splitting in monolayer MoS_2 can be achieved by the magnetic proximity effect of an antiferromagnetic insulating CoO(111) substrate. The effective Zeeman magnetic field caused by the CoO substrate is 8.8 meV (i.e., 152 T). This leads to a spin splitting of 0.32 eV at the K valley and 0.19 eV at the K' valley, and the resulting valley splitting is 103 meV, which mainly originates from the contributions of the Mo d_{xy} and $d_{x^2-y^2}$ states. The calculated Berry curvature has the same magnitude but opposite signs for the K and K' valleys, which indicates that the heterostructure retains the characteristic of a valley, in contrast to monolayer MoS_2.

The opposite Berry curvatures at the two valleys will lead to opposite transverse velocities of the carriers with application of an in-plane longitudinal electric field, so we propose a valleytronic device based on the MoS_2/CoO(111) heterostructure. In this device, the carriers are spin-up holes at the K valley and they move to the upside edge of the device if the interfacial Co atoms have an up magnetic moment. However, the carriers change to spin-down holes at the K' valley and move to the downside edge of the device if the interfacial Co atoms have a down magnetic moment. This realizes filtering of both the valley and spin because the carriers are spin up for the two opposite magnetic Zeeman fields. The magnetic proximity effect provided by the antiferromagnetic insulator can break the time-reversal symmetry of MoS_2, which leads to prominent valley splitting. The direct result of breaking of the time-reversal symmetry is the appearance of AHC. The AHC in the range -1.53 eV (VBM of K) to -1.62 eV (VBM of K') shows a quantized character, which is theoretically confirmed based on the 2D electron gas formalism and semiclassical equations for electrons in magnetic Bloch bands. This study suggests that using a type-II antiferromagnetic insulator as a magnetic substrate is effective for causing valley splitting by the magnetic proximity effect because the magnetic moments of the magnetic atoms in one layer of the (111) plane are arranged in the same direction. This approach can be applied to design a new class of magnetic substrates that can control the spin and valley splitting, and has potential applications in the valley anomalous Hall effect.

ACKNOWLEDGMENTS

We would like to acknowledge the support by the National Natural Science Foundation of China (Grant No. 61671199), the China Postdoctoral Science Foundation (Grant No. 2016M601243), the Advanced Foundation of Postdoctoral Research of Hebei Province (Grant No. B2016005002), the Chunhui Program (Grant No. Z2017024), and the National Key Research and Development Program of China (Grant No. 2017YFA0206303, MOST of China).

[1] A. Rycerz, J. Tworzydło, and C. W. J. Beenakker, Nat. Phys. **3**, 172 (2007).
[2] D. Xiao, M.-C. Chang, and Q. Niu, Rev. Mod. Phys. **82**, 1959 (2010).
[3] X. Xu, W. Yao, D. Xiao, and T. F. Heinz, Nat. Phys. **10**, 343 (2014).
[4] D. Xiao, G.-B. Liu, W. X. Feng, X. D. Xu, and W. Yao, Phys. Rev. Lett. **108**, 196802 (2012).
[5] W. X. Feng, Y. G. Yao, W. G. Zhu, J. J. Zhou, W. Yao, and D. Xiao, Phys. Rev. B **86**, 165108 (2012).
[6] O. Gunawan, Y. P. Shkolnikov, K. Vakili, T. Gokmen, E. P. De Poortere, and M. Shayegan, Phys. Rev. Lett. **97**, 186404 (2006).
[7] D. Xiao, W. Yao, and Q. Niu, Phys. Rev. Lett. **99**, 236809 (2007).
[8] Z. Y. Zhu, Y. C. Cheng, and U. Schwingenschlögl, Phys. Rev. B **84**, 153402 (2011).
[9] Y. C. Cheng, Q. Y. Zhang, and U. Schwingenschlögl, Phys. Rev. B **89**, 155429 (2014).
[10] W. Yao, D. Xiao, and Q. Niu, Phys. Rev. B **77**, 235406 (2008).
[11] H. L. Zeng, J. F. Dai, W. Yao, D. Xiao, and X. D. Cui, Nat. Nanotechnol. **7**, 490 (2012).
[12] E. J. Sie, J. W. McIver, Y.-H. Lee, L. Fu, J. Kong, and N. Gedik, Nat. Mater. **14**, 290 (2015).
[13] K. F. Mak, K. L. McGill, J. Park, and P. L. McEuen, Science **344**, 1489 (2014).
[14] J. Lee, K. F. Mak, and J. Shan, Nat. Nanotechnol. **11**, 421 (2016).
[15] Y. L. Li, J. Ludwig, T. Low, A. Chernikov, X. Cui, G. Arefe, Y. D. Kim, A. M. van der Zande, A. Rigosi, H. M. Hill, S. H. Kim, J. Hone, Z. Q. Li, D. Smirnov, and T. F. Heinz, Phys. Rev. Lett. **113**, 266801 (2014).
[16] G. Aivazian, Z. R. Gong, A. M. Jones, R.-L. Chu, J. Yan, D. G. Mandrus, C. Zhang, D. Cobden, W. Yao, and X. Xu, Nat. Phys. **11**, 148 (2015).
[17] A. Srivastava, M. Sidler, A. V. Allain, D. S. Lembke, A. Kis, and A. Imamoglu, Nat. Phys. **11**, 141 (2015).
[18] D. MacNeill, C. Heikes, K. F. Mak, Z. Anderson, A. Kormányos, V. Zólyomi, J. Park, and D. C. Ralph, Phys. Rev. Lett. **114**, 037401 (2015).
[19] G. Wang, L. Bouet, M. M. Glazov, T. Amand, E. L. Ivchenko, E. Palleau, X. Marie, and B. Urbaszek, 2D Mater. **2**, 034002 (2015).
[20] M. Koperski, K. Nogajewski, A. Arora, V. Cherkez, P. Mallet, J.-Y. Veuillen, and J. Marcus, Nat. Nanotechnol. **10**, 503 (2015).
[21] G.-B. Liu, D. Xiao, Y. G. Yao, X. D. Xu, and W. Yao, Chem. Soc. Rev. **44**, 2643 (2015).
[22] J. R. Schaibley, H. G. Yu, G. Clark, P. Rivera, J. S. Ross, K. L. Seyler, W. Yao, and X. D. Xu, Nat. Rev. Mater. **1**, 160551 (2016).
[23] C. E. Nebel, Nat. Mater. **12**, 690 (2013).
[24] T. Cao, G. Wang, W. P. Han, H. Q. Ye, C. R. Zhu, J. R. Shi, Q. Niu, P. H. Tan, E. G. Wang, B. L. Liu, and J. Feng, Nat. Commun. **3**, 887 (2012).
[25] K. F. Mak, K. He, J. Shan, and T. F. Heinz, Nat. Nanotechnol. **7**, 494 (2012).
[26] Y. C. Cheng, Z. Y. Zhu, W. B. Mi, Z. B. Guo, and U. Schwingenschlögl, Phys. Rev. B **87**, 100401 (2013).
[27] J. S. Qi, X. Li, Q. Niu, and J. Feng, Phys. Rev. B **92**, 121403 (2015).
[28] Q. Y. Zhang, S. A. Yang, W. B. Mi, Y. C. Cheng, and U. Schwingenschlögl, Adv. Mater. **28**, 959 (2016).
[29] Y. Song, Q. Zhang, W. B. Mi, and X. C. Wang, Phys. Chem. Chem. Phys. **18**, 15039 (2016).
[30] Y. Song, W. B. Mi, and X. C. Wang, Adv. Mater. Interfaces **3**, 1600581 (2016).
[31] C. Zhao, T. Z. Norden, P. Y. Zhang, P. Q. Zhao, Y. C. Cheng, F. Sun, J. P. Parry, P. Taheri, J. Q. Wang, Y. H. Yang, T. Scrace, K. Kang, S. Yang, G.-X. Miao, R. Sabirianov, G. Kioseoglou, W. Huang, A. Petrou, and H. Zeng, Nat. Nanotechnol. **12**, 757 (2017).

[32] X. Liang, L. J. Deng, F. Huang, T. T. Tang, C. T. Wang, Y. P. Zhu, J. Qin, Y. Zhang, B. Peng, and L. Bi, Nanoscale **9**, 9502 (2017).
[33] D. Zhong, K. L. Seyler, X. Linpeng, R. Cheng, N. Sivadas, B. Huang, E. Schmidgall, T. Taniguchi, K. Watanabe, M. A. McGuire, W. Yao, D. Xiao, Kai-M. C. Fu, and X. Xu, Sci. Adv. **3**, e1603113 (2017).
[34] L. Xu, M. Yang, L. Shen, J. Zhou, T. Zhu, and Y. P. Feng, Phys. Rev. B **97**, 041405 (2018).
[35] K. L. Seyler, D. Zhong, B. Huang, X. Linpeng, N. P. Wilson, T. Taniguchi, K. Watanabe, W. Yao, D. Xiao, M. A. McGuire, K.-M. C. Fu, and X. Xu, Nano Letters **18**, 3823 (2018).
[36] Z. H. Zhang, X. F. Liu, J. Yu, Y. Hang, Y. Li, Y. F. Guo, Y. Xu, X. Sun, J. X. Zhou, and W. L. Guo, Comput. Mol. Sci. **6**, 324 (2016).
[37] A. V. Stier, K. M. McCreary, B. T. Jonker, J. Kono and S. A. Crooker, Nat. Commun. **7**, 10643 (2016).
[38] P. S. Silinsky and M. S. Seehra, Phys. Rev. B **24**, 419 (1981).
[39] L. Q. Wang, J. Y. Zhang, Z. X. Zeng, Y. M. Lin, L. T. Hu, and Q. J. Xue, Nanotechnology **17**, 4614 (2006).
[40] W. Meyer, K. Biedermann, M. Gubo, L. Hammer, and K. Heinz, Phys. Rev. B **79**, 121403 (2009).
[41] G. Kresse and J. Furthmüller, Phys. Rev. B **54**, 11169 (1996).
[42] J. P. Perdew, K. Burke, and M. Ernzerhof, Phys. Rev. Lett. **77**, 3865 (1996).
[43] G. Kresse, J. Furthmüller, and J. Hafner, Phys. Rev. B **50**, 13181 (1994).
[44] M. Fuchs, and M. Scheffler, Comput. Phys. Commun. **119**, 67 (1999).
[45] P. E. Blöchl, Phys. Rev. B **50**, 17953 (1994).
[46] G. Kresse and D. Joubert, Phys. Rev. B **59**, 1758 (1999).
[47] S. Grimme, J. Comput. Chem. **25**, 1463 (2004).
[48] A. A. Mostofi, Comput. Phys. Commun. **178**, 685 (2008).
[49] Q. H. Wang, K. Kalantar-Zadeh, A. Kis, J. N. Coleman, and M. S. Strano, Nat. Nanotechnol. **7**, 699 (2012).
[50] S. Helveg, J. V. Lauritsen, E. Lægsgaard, I. Stensgaard, J. K. Nørskov, B. S. Clausen, H. Topsøe, and F. Besenbacher, Phys. Rev. Lett. **84**, 951 (2000).
[51] U. D. Wdowik, and K. Parlinski, Phys. Rev. B **75**, 104306 (2007).
[52] J. van Elp, J. L. Wieland, H. Eskes, P. Kuiper, G. A. Sawatzky, F. M. F. de Groot, and T. S. Turner, Phys. Rev. B **44**, 6090 (1991).
[53] M. Born and K. Huang, *Dynamical Theory of Crystal Lattices* (Oxford University Press, Oxford, 1954).
[54] T. Y. Cai, S. A. Yang, X. Li, F. Zhang, J. R. Shi, W. Yao, and Q. Niu, Phys. Rev. B **88**, 115140 (2013).
[55] X. Wang, J. R. Yates, I. Souza, and D. Vanderbilt, Phys. Rev. B **74**, 195118 (2006).
[56] Y. G. Yao, L. Kleinman, A. H. MacDonald, J. Sinova, T. Jungwirth, D.-S. Wang, E. G. Wang, and Q. Niu, Phys. Rev. Lett. **92**, 037204 (2004).
[57] D. J. Thouless, M. Kohmoto, M. P. Nightingale, and M. den Nijs, Phys. Rev. Lett. **49**, 405 (1982).
[58] M. C. Chang and Q. Niu, Phys. Rev. Lett. **75**, 1348 (1995).